OPTICA

Dissipative Kerr solitons in integrated Fabry–Perot microresonators

THIBAULT WILDI,[1] MAHMOUD A. GAAFAR,[1] THIBAULT VOUMARD,[1] MARKUS LUDWIG,[1] AND TOBIAS HERR[1,2,*]

[1]Deutsches Elektronen-Synchrotron DESY, Notkestr. 85, 22607 Hamburg, Germany
[2]Physics Department, Universität Hamburg UHH, Luruper Chaussee 149, 22761 Hamburg, Germany
*tobias.herr@desy.de

Received 17 November 2022; revised 7 April 2023; accepted 11 April 2023; published 23 May 2023

Dissipative Kerr solitons (DKSs) in integrated microresonators have enabled breakthroughs in sensing, communication, and signal processing. So far, integrated DKS sources have relied exclusively on ring-type resonators where the resonator's dispersion is defined by its waveguide. Means of engineering the dispersion that go beyond modifying the waveguide's cross section are needed for accessing new wavelength and operating regimes. Here, we demonstrate DKS generation from a continuous-wave driving-laser in an integrated Fabry–Perot microresonator. In this topology, the dispersion is not dominated by the waveguide but by nanostructured photonic crystal mirrors. Leveraging wafer-level fabrication, high intrinsic Q-factors of 4 million are achieved and unintentional avoided mode crossings that can prevent DKS formation are absent. This establishes an integrated resonator topology for DKS generation and creates opportunities for alternative wavelength domains and approaches such as dispersion managed solitons or Nyquist solitons.

https://doi.org/10.1364/OPTICA.480789

1. INTRODUCTION

Dissipative Kerr solitons (DKSs) [1–4] in laser-driven dielectric microresonators provide access to metrology-grade femtosecond sources and broadband frequency combs with repetition rates from tens of GHz to multiple THz. They are self-enforcing solutions to the Lugiato–Lefever equation (LLE) and can emerge in *high-quality factor* (Q) microresonators from the balance between *anomalous* group delay dispersion (GDD), loss, and Kerr nonlinearity under (typically) continuous-wave (CW) laser driving. Intriguing nonlinear dynamics including soliton crystals [5], soliton molecules [6], synchronization between resonators [7], and discrete photonic time crystals [8] have been observed. Owing to their potential for compact photonic integration [4,9], DKS sources are a transformative technology, impacting a wide range of cross-disciplinary applications, including data transmission [10] and processing [11], ranging [12,13], microwave photonics [14], dual-comb spectroscopy [15], and astronomical spectrograph calibration [16,17]. To date, integrated DKS sources have been pursued exclusively in traveling-wave ring-type resonators. Here, criteria for DKS formation can be routinely met, including high Q-factor, anomalous dispersion (negative GDD), as well as a resonance spectrum free of unintentional avoided mode crossings (AMXs) [18]. Furthermore, the dispersion can be tuned (to some extent) by adjusting the width and height of the resonator waveguide, with significant impact on DKSs and their spectra. Future extension of DKS technology, including extension to new wavelength regimes (e.g., visible wavelengths), spectral engineering, as well as exploration of new operating regimes (e.g., dispersion managed [19–21], sinc-, Nyquist-, and zero-dispersion solitons [22–24]), will critically rely on the development of new approaches for dispersion engineering. Importantly, these modifications should be broadband (across hundreds of resonator modes), without jeopardizing the high Q-factor and without inducing unintentionally AMXs.

Advanced techniques for *narrowband* dispersion modification in DKS-generating ring-type microresonators have been demonstrated including shifting of few resonance frequencies via mode coupling between cross-polarized modes [25], fundamental and higher-order transverse modes [26], counterpropagating modes in corrugated resonators [27], as well as mode hybridization in concentric resonators [28] and between modes in distinct resonators [29,30]; these techniques have led to deterministic initiation of DKSs, higher-power efficiency, and novel nonlinear phenomena. Recently, the approach of coupling between counterpropagating modes in corrugated waveguide resonators has been extended, with single-mode control, to tens of resonator modes through inverse design [31] and Fourier synthesis [32], representing a significant step in broadband dispersion engineering that may enable DKS in the future.

Complementary to methods developed for ring-type devices, Fabry–Perot (FP) microresonators with dispersive mirrors

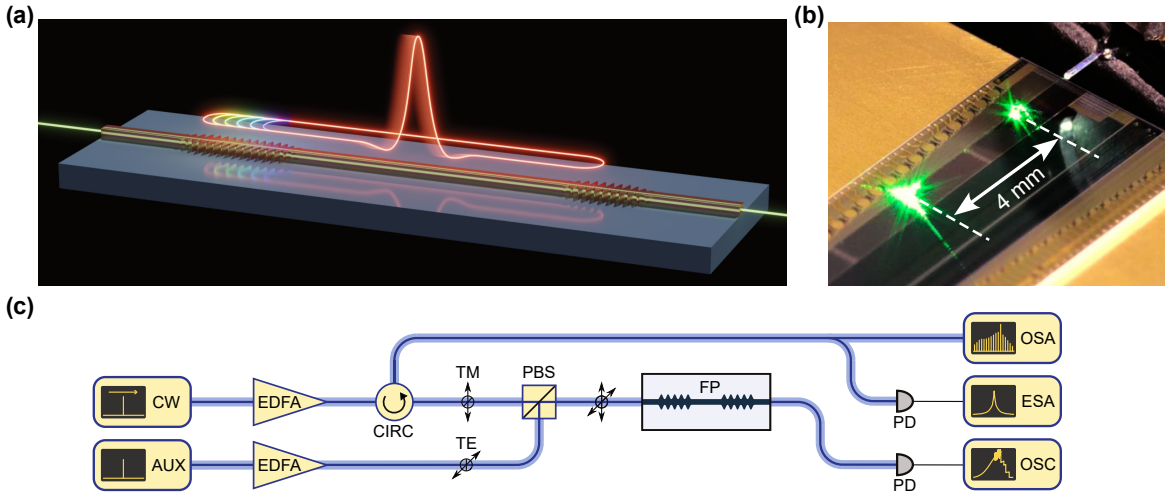

Fig. 1. Soliton generation in chip-integrated photonic crystal Fabry–Perot cavities. (a) Illustration of a dissipative Kerr soliton (DKS) under continuous-wave pumping inside a chip-integrated photonic crystal Fabry–Perot (FP) microresonator with reflector-induced anomalous dispersion. (b) Photograph of a CW-driven FP microresonator. Scattered coincidental third-harmonic generation indicates the position of the PCRs. (c) Setup for exciting DKSs inside the FP microresonator. A transverse magnetic (TM) polarized continuous-wave (CW) pump laser is tuned into resonance while the resonator is thermally stabilized by an auxiliary continuous-wave laser (AUX) in the transverse electric (TE) mode. EDFA, erbium-doped fiber amplifier; CIRC, circulator; PBS, polarizing beam splitter; PD, photodetector; OSC, oscilloscope; ESA, electrical spectrum analyzer; OSA, optical spectrum analyzer.

represent an attractive approach to broadband dispersion engineering: nearly 30 years ago, the advent of suitably designed Bragg mirrors for ultrafast lasers represented a breakthrough in the field when faced with a similar challenge [33,34]. So far, Bragg mirrors have also been applied to short-fiber-based FP microresonators resulting in four-wave mixing and stimulated Brillouin scattering [35], as well as the first demonstration of pulse-driven DKS [36]. Notably, recent advances led to the first integrated FP resonator with photonic crystal mirrors for comb generation [37] as well as FP microresonators with dispersion engineered reflecting structures, based on inverse design [38]. Despite all these major advances, a DKS-supporting platform whose broadband dispersion is not limited to effective waveguide (or whispering-gallery mode) dispersion has not yet been demonstrated.

Here, we demonstrate for the first time DKS generation in an integrated FP microresonator. Fabricated using a wafer-scale process, the microresonator is composed of two photonic crystal reflectors (PCRs) in a waveguide [Fig. 1(a)]. Significantly, across its entire bandwidth the dispersion of the resonator is dominated by the GDD contribution from the PCRs (not the waveguide), demonstrating new opportunities for dispersion engineering in a system capable of supporting DKSs. Further, the FP microresonator's intrinsic Q-factor, albeit not record high for an integrated device [39,40], is on par with ring resonators fabricated in the same commercial platform. Our results establish integrated FP resonators as a powerful complement to ring resonators.

2. RESONATOR DESIGN AND FABRICATION

The FP resonators are fabricated on-chip in a 800 nm thick silicon nitride layer and embedded in a fused silica cladding. The two PCRs are implemented as submicrometer-scale sinusoidal corrugations in a waveguide. Each corrugation period corresponds to a unit cell of the PCR, which is characterized by its length, mean width, and corrugation depth [Fig. 2(a) ①]. The periodic corrugation induces a photonic bandgap that defines the PCR's reflection bandwidth [Fig. 2(b)]; the length of the PCRs (∼100 units cell per reflector) defines the reflectivity and thus the coupling strength to the waveguide that extends beyond the resonator to the chip's facets for light coupling. Alternatively, evanescent coupling can be used, although the coupler is then encountered twice per round-trip, increasing the effective internal loss rate of the cavity (cf. Supplement 1). To design the PCRs, we employ finite element modeling to map the unit cell parameters to the photonic bandgap's opening and central frequency [Fig. 2(c)], which permits choosing the desired parameters. In the present case, we choose a constant unit cell for the main region of the PCR to create a bandgap centered around 1570 nm, the middle wavelength of our tunable CW pump laser. Note that in principle each unit cell could have a different set of defining parameters, creating a large design space and permitting crafting of highly customized resonators. An adiabatic taper [Fig. 2(a) ②] connects the PCRs on both sides to an uncorrugated waveguide and suppresses losses due to the overlap mismatch between the fundamental guided mode of the uncorrugated waveguide and the PCR's fundamental Bloch mode [41,42]. Transitioning from the PCR to the uncorrugated waveguide proceeds by gradually reducing the corrugation depth while simultaneously adjusting the mean width such that the bandgap center frequency is kept constant [43]. Finally, upon reaching zero-corrugation, the waveguide linearly tapers up to a width of 1.6 μm over a length of 200 μm to reduce propagation losses from sidewall-roughness scattering while still keeping a strong mode confinement [Fig. 2(a) ③]. A 3400 μm long waveguide section forms the resonator cavity between the 2 PCRs [Fig. 2(a) ④], defining the resonator's free-spectral range (FSR), in this case ∼19 GHz, which is within the K-frequency band and directly detectable by a photodiode and a microwave spectrum analyzer.

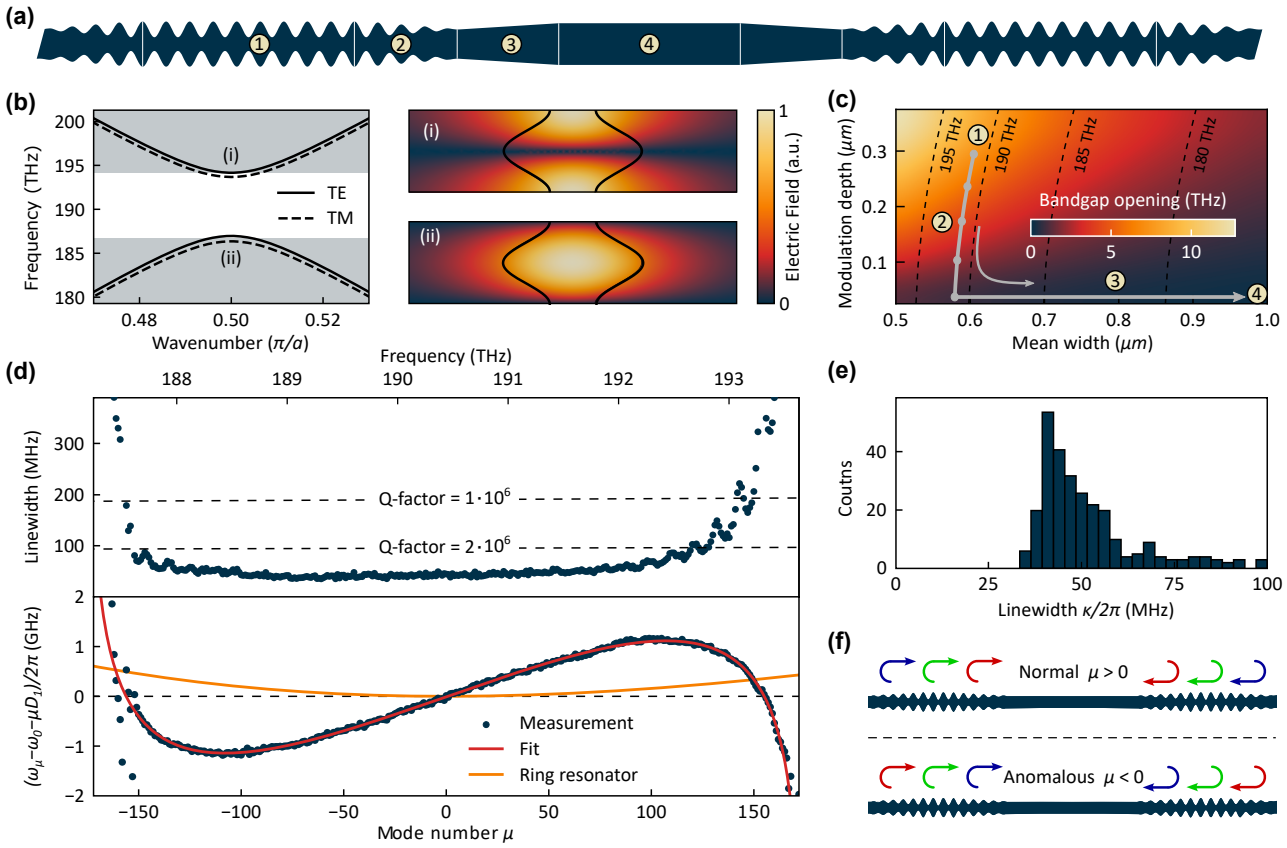

Fig. 2. Design of photonic crystal Fabry–Perot cavities. (a) Schematic of a photonic crystal Fabry–Perot (FP) microresonator (not to scale), composed of photonic crystal reflectors (PCRs) ①, adiabatic tapers ②, linear tapers ③, and intracavity waveguide ④. (b) Left panel: illustration of a photonic band diagram for transverse electric (TE) and transverse magnetic (TM) modes. The wavenumber is given in units of π/a, where a is the unit cell length. The bandgap, i.e., reflection bandwidth, is highlighted in white. Right panels: TM mode profiles (electric field strength) of upper and lower frequency modes of an example PCR unit cell with the corresponding cell contour overlaid in black (data based on finite element modeling). (c) Map of the TM bandgap opening and center frequency as function of corrugation depth and mean width of the lattice cell for a fixed PCR period (i.e. cell length) of 475 nm (data based on finite element modeling). The PCR can be described by its trajectory through this design space (where the third dimension, cell length, is not shown). (d) TM mode family. Upper panel: measured resonance linewidths as function of relative mode number μ (cf. main text). Lower panel: measured dispersion (cf. main text) of a photonic crystal FP resonator with a mean free-spectral range $\overline{\mathrm{FSR}} = D_1/2\pi = 18.55$ GHz. For comparison, the dispersion of an equivalent ring resonator with the same $\overline{\mathrm{FSR}}$ and waveguide cross section identical to the FP's intracavity waveguide is plotted in orange, corresponding to the intracavity waveguide contribution to the FP resonator's total dispersion. A fit based on a coupled-mode description of the PCRs is shown in red (cf. Supplement 1). (e) Histogram of the intrinsic resonance linewidths from (d) with a median value of 47 MHz corresponding to an intrinsic Q-factor of 4 million. (f) Normal (anomalous) round-trip GDD corresponds to an increasing (decreasing) effective resonator length with increasing frequency.

3. EXPERIMENTS

To characterize the fabricated resonators, we first measure the intrinsic linewidths in a strongly undercoupled resonator [Fig. 2(d)]; undercoupling assesses the intrinsic cavity loss and permits a direct comparison to (equally undercoupled) ring-type resonators fabricated through the same process. The PCR unit cell of this resonator is designed to have a period of 475 nm, width of 600 nm, and corrugation depth of 300 nm. Owing to the narrow width of the unit cell, the PCR supports only the fundamental TE and TM modes, which is desirable for reproducible resonator characteristics. The resonator's spectrum extends over 300 longitudinal modes, and an intrinsic linewidth of 100 MHz or below is maintained over a bandwidth of 5 THz (40 nm), sufficient to support ultrashort femtosecond pulses. The median intrinsic (undercoupled) linewidth over the mirror bandwidth (here, defined as the spectral interval where the linewidth is consistently below 100 MHz) is 47 MHz [Fig. 2(e)]. This corresponds to a median intrinsic Q-factor of $4.0 \cdot 10^6$, which is limited only by the $\sim$0.1 dB cm^{-1} propagation loss inherent to the commercial platform used to fabricate the samples (cf. Supplement 1), and thus on par with ring resonators fabricated through the same commercial wafer-scale process.

Next, we measure the resonator's dispersion as shown in Fig. 2(d) in terms of the integrated dispersion $D_{\mathrm{int}} = \omega_\mu - \omega_0 - \mu D_1$, which quantifies the deviation of the resonance frequencies ω_μ from a dispersion-free equidistant frequency grid as a function of the relative mode number μ. In this representation, anomalous (normal) dispersion appears as a convex (concave) curve. The strength of the local dispersion at a specific frequency can be estimated by choosing $D_1/(2\pi)$ to be the local FSR and expand $D_{\mathrm{int}} \approx \frac{1}{2}\mu^2 D_2$ around this frequency. Anomalous (normal) dispersion is then indicated by positive (negative) D_2. Here, μ is chosen such that $\mu = 0$ coincides with the center of the reflector's bandwidth, and $D_1/(2\pi)$ is chosen to be approximately the average $\overline{\mathrm{FSR}}$ over the reflector's bandwidth. For comparison, Fig. 2(d) also shows the dispersion curve of an equivalent ring-type

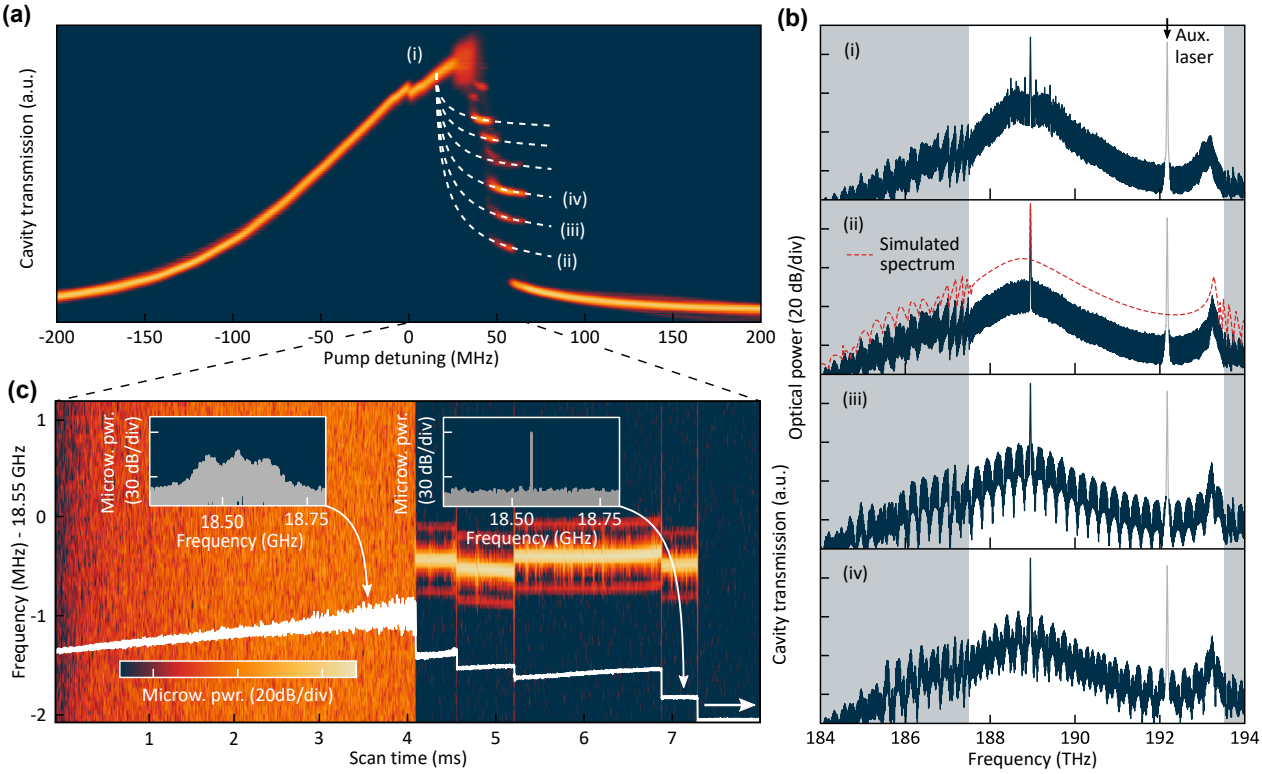

Fig. 3. Dissipative Kerr soliton in a photonic crystal Fabry–Perot resonator. (a) Heat-map compiled from 100 transmission traces, highlighting multiple possible intracavity power evolutions as a function of pump detuning. The step-like features present at ∼50 MHz detuning indicate quantized power levels, a canonical signature of DKS formation. (b) Optical spectra of modulation instability (i), single- (ii), two- (iii) and three- (iv) soliton states. A dispersive wave is present on the blue side of the spectra, due to the local presence of strong normal dispersion. The auxiliary laser's line (cf. Supplement 1), is grayed out for clarity; the nominal PCR bandwidth is highlighted in white. The spectrum obtained from numerical simulations based on the measured cavity parameters (cf. Supplement 1) is shown in red, offset by +10 dB, corresponding to a pulse of ∼300 fs. (c) Spectrogram showing the evolution of the mirowave beatnote signal (∼18.5 GHz) as a function of pump detuning. Overlayed in white is the corresponding resonator transmission signal. The insets show the beatnote in the modulation instability and soliton regime (resolution bandwidth: 100 kHz).

resonator (with the same $\overline{\mathrm{FSR}}$, same waveguide cross section as the FP intracavity waveguide, and negligible effect of curvature on dispersion), corresponding to the intracavity waveguide contribution to the FP resonator's total dispersion; the marked difference between both dispersion curves shows the dominating impact of the PCRs on the FP resonator's dispersion. The exact contribution of the PCRs to the dispersion can be calculated through their complex reflection coefficient (cf. Supplement 1), which matches well the observations [also indicated in Fig. 2(d) as "Fit"]. With the current PCR design, the resonator provides both normal and anomalous dispersion regimes, independent of the anomalous background contribution from the intracavity waveguide. This may be understood as a wavelength-dependent effective reflection depth in the PCRs [Fig. 2(f)].

Moreover, the measured dispersion of the resonance frequencies in Fig. 2(d) is free of strong local deviations such as AMXs, which can arise from coupling between frequency degenerate counter-propagating modes or coupling between different transverse mode families. Here, these two mechanisms are absent: in contrast to rings, the FP resonator has no distinct counterpropagating mode, which leads to the striking absence of unintentional mode splitting often observed in rings (cf. Supplement 1); higher-order transverse modes are efficiently suppressed by the single-mode nature of the PCRs. These features contribute to achieving a smooth anomalous dispersion, which in conjunction with the high-Q provides favorable conditions for DKS formation [18].

To generate DKSs, a more strongly coupled resonator with a 15% shorter input PCR (but with otherwise identical geometry) and a 56 MHz median total linewidth is used for more efficient operation. The setup for this experiment is shown in Fig. 1(c): the resonator is pumped using a tunable laser in TM polarization in the anomalous dispersion regime (local $D_2/(2\pi) = 210$ kHz) at a wavelength of 1587 nm (188.9 THz). Repeatedly scanning the pump laser (150 mW on-chip) from blue- to red-detuned across a resonance, we record the resonator transmission signals and superpose them in Fig. 3(a). After an initial modulation instability (MI) state (i), characteristic step features (ii–iv, etc.) are visible, which are indicative of DKS formation [2], each step corresponding to an integer numbers of solitons in the resonator that can be generated during a laser scan. The corresponding MI spectrum, the comb spectrum of a single soliton, as well as more structured comb spectra of multiple-soliton states are shown in Fig. 3(b), where the white background highlights the nominal PCR bandwidth. Initially, all spectra exhibit a periodic modulation of their envelopes caused by reflections between the PCR and chip facet, which has been removed before plotting (cf. Supplement 1); although of no concern here, the modulation could be avoided by anti-reflection coating the chip's facet, index-matching fluid, or

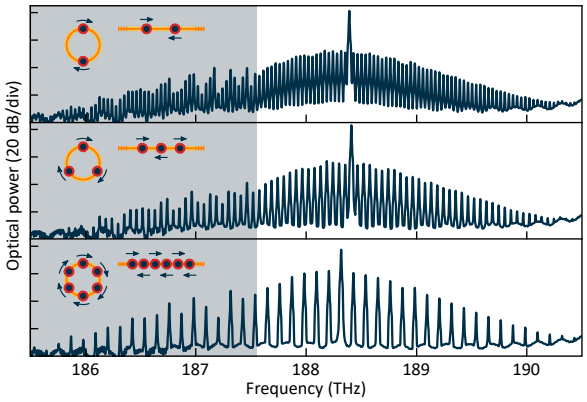

Fig. 4. Recorded spectra of two-, three-, and 6-soliton crystal states obtained by pumping at slightly different frequencies. The PCR's nominal bandwidth is highlighted by a white background. A snap-shot crystalline distribution of DKSs in a linear FP cavity is shown as an inset along with an equivalent ring configuration.

evanescent waveguide coupling if necessary. From fitting the single DKS's spectrum with a sech^2 envelope [Fig. 3(b) (ii)], we estimate the transform-limited soliton pulse duration to be ∼300 fs. Close to the blue edge of the resonator's bandwidth, we observe a dispersive wave [44] as expected from the normal dispersion in this spectral region. Due to a relaxed phase-matching condition outside the high-reflectivity bandwidth, all spectra extend beyond the nominal PCR bandwidth, strongly modulated by the sidelobes of the PCRs (cf. Supplement 1). To further confirm DKS generation, we record the microwave pulse repetition rate beatnote as a function of detuning [Fig. 3(c)]. As expected, the beatnote transitions from a high-noise to a narrow-linewidth signal, when entering into a DKS state (with each subsequent transition to a lower number of solitons corresponding to a slight change of the repetition rate). Finally, we also observe the formation of soliton crystals [5] [Fig. 4], a state commonly observed in traveling-wave microresonators where a self-organized train of equidistant soliton pulses circulates inside the resonator, (effectively increasing the pulse repetition rate and hence the comb line spacing by an integer factor). These observations further establish the standing-wave FP resonator as a DKS platform and strengthen the link to traveling-wave ring-type resonators.

Indeed, the nonlinear dynamics of standing-wave resonators is similar to the traveling-wave case, with an additional phase shift due to cross-phase modulation between counterpropagating waves proportional to the average intracavity power [36,45]; this effect can be compensated for by a slight change in the pump laser detuning. Different from a conventional ring-type resonator, the dispersion in the present resonator includes localized and distributed contributions from the PCRs and the connecting waveguide, respectively (cf. Supplement 1). Here, as both a single reflection off of a PCR and single propagation through the waveguide have negligible effect on the DKS pulse, they can be lumped together. This implies that established mean-field models for ring resonators can also be used for describing the present FP resonators, with the inclusion of the aforementioned phase shift.

Complementing the experimental study of DKS formation in the new resonator platform, we perform numeric simulations based on the frequency-domain formulation of the LLE [46,47], which readily permits inclusion of the spectrally dependent measured dispersion and linewidths (cf. Supplement 1). The simulated spectrum is overlayed with the experimental single-soliton spectrum in panel (ii) of Fig. 3(b), reproducing all spectral features with remarkable fidelity, including the dispersive wave and the spectral extension beyond the nominal PCR bandwidth.

4. DISCUSSION

In summary, we have shown for the first time DKS formation in a chip-integrated FP resonator. The resonator's dispersion is not defined by waveguide dispersion, but by its PCR mirrors. Through careful design, we achieve a high intrinsic Q-factor of 4 million, matching that of traveling-wave-type resonators fabricated in the same wafer-scale commercial foundry process. The absence of distinct frequency degenerate counterpropagating modes in the FP geometry and the single-mode nature of the PCRs avoids unintentionally AMXs that can inhibit DKS formation. Under CW driving, we observe single and multiple (hence colliding) DKS pulses, as well as soliton crystals states. This establishes integrated FP resonators as a new topology for DKS generation that can add to and complement existing ring-resonator-based approaches. As each unit cell of the PCRs can, in principle, be individually adjusted, this opens a large design space for future tailoring of dispersion, spectrally dependent Q-factors and filters, bandwidth extension through chirped reflectors or broadband phase matching, while allowing for compact integration. Future efforts may benefit from insights obtained in the context of mirrors for ultrafast lasers [33,34] and inverse design approaches [31,38]. With relevance to quantum photonics, bio-chemical sensing, and astronomical spectrograph calibration, the presented results provide a resonator platform that, through customized PCRs, may lead to DKSs at visible wavelengths, and at other wavelengths that are currently inaccessible due to unsuitable effective waveguide dispersion. Besides DKS, the integrated FP platform could also prove useful for microresonator frequency combs via cascaded four-wave mixing [48] and switching waves [49–51], as well as integrated optical parametric oscillators [52] and optical harmonic generation [53]. Immediate further research opportunities leveraging the specific characteristics of the new resonators include dispersion managed solitons [19–21], sinc-, Nyquist-, and zero-dispersion solitons [22–24], nonlinear "gain-through-loss" [54], slow light [55], spectral engineering [31,32], and filter-driven pulse formation [56,57], which bodes well for integrated broadband and ultrafast light sources.

Funding. European Research Council under the EU's Horizon 2020 research and innovation program (853564); EU Horizon 2020 Framework Programme (965124); Helmholtz Young Investigators Group (VH-NG-1404).

Acknowledgment. The authors acknowledge valuable discussions with Alexander Yu. Petrov regarding the analytic computation of the PCR's dispersion (cf. Supplement 1). The work was supported through the Maxwell computational resources operated at DESY.

Disclosures. The authors declare no conflicts of interest.

Data availability. Data underlying the results presented in this paper are not publicly available at this time but may be obtained from the authors upon reasonable request.

Supplemental document. See Supplement 1 for supporting content.

REFERENCES

1. F. Leo, S. Coen, P. Kockaert, S.-P. Gorza, P. Emplit, and M. Haelterman, "Temporal cavity solitons in one-dimensional Kerr media as bits in an all-optical buffer," Nat. Photonics **4**, 471–476 (2010).

2. T. Herr, V. Brasch, J. D. Jost, C. Y. Wang, N. M. Kondratiev, M. L. Gorodetsky, and T. J. Kippenberg, "Temporal solitons in optical microresonators," Nat. Photonics **8**, 145–152 (2014).
3. T. J. Kippenberg, A. L. Gaeta, M. Lipson, and M. L. Gorodetsky, "Dissipative Kerr solitons in optical microresonators," Science **361**, eaan8083 (2018).
4. A. L. Gaeta, M. Lipson, and T. J. Kippenberg, "Photonic-chip-based frequency combs," Nat. Photonics **13**, 158–169 (2019).
5. D. C. Cole, E. S. Lamb, P. Del'Haye, S. A. Diddams, and S. B. Papp, "Soliton crystals in Kerr resonators," Nat. Photonics **11**, 671–676 (2017).
6. W. Weng, R. Bouchand, E. Lucas, E. Obrzud, T. Herr, and T. J. Kippenberg, "Heteronuclear soliton molecules in optical microresonators," Nat. Commun. **11**, 2402 (2020).
7. J. K. Jang, A. Klenner, X. Ji, Y. Okawachi, M. Lipson, and A. L. Gaeta, "Synchronization of coupled optical microresonators," Nat. Photonics **12**, 688–693 (2018).
8. H. Taheri, A. B. Matsko, L. Maleki, and K. Sacha, "All-optical dissipative discrete time crystals," Nat. Commun. **13**, 848 (2022).
9. J. S. Levy, A. Gondarenko, M. A. Foster, A. C. Turner-Foster, A. L. Gaeta, and M. Lipson, "CMOS-compatible multiple-wavelength oscillator for on-chip optical interconnects," Nat. Photonics **4**, 37–40 (2010).
10. P. Marin-Palomo, J. N. Kemal, M. Karpov, A. Kordts, J. Pfeifle, M. H. P. Pfeiffer, P. Trocha, S. Wolf, V. Brasch, M. H. Anderson, R. Rosenberger, K. Vijayan, W. Freude, T. J. Kippenberg, and C. Koos, "Microresonator-based solitons for massively parallel coherent optical communications," Nature **546**, 274–279 (2017).
11. M. Tan, X. Xu, J. Wu, R. Morandotti, A. Mitchell, and D. J. Moss, "RF and microwave photonic temporal signal processing with Kerr micro-combs," Adv. Phys.: X **6**, 1838946 (2021).
12. P. Trocha, M. Karpov, D. Ganin, M. H. P. Pfeiffer, A. Kordts, S. Wolf, J. Krockenberger, P. Marin-Palomo, C. Weimann, S. Randel, W. Freude, T. J. Kippenberg, and C. Koos, "Ultrafast optical ranging using microresonator soliton frequency combs," Science **359**, 887–891 (2018).
13. M.-G. Suh and K. J. Vahala, "Soliton microcomb range measurement," Science **359**, 884–887 (2018).
14. E. Lucas, P. Brochard, R. Bouchand, S. Schilt, T. Südmeyer, and T. J. Kippenberg, "Ultralow-noise photonic microwave synthesis using a soliton microcomb-based transfer oscillator," Nat. Commun. **11**, 374 (2020).
15. M.-G. Suh, Q.-F. Yang, K. Y. Yang, X. Yi, and K. J. Vahala, "Microresonator soliton dual-comb spectroscopy," Science **354**, 600–603 (2016).
16. E. Obrzud, M. Rainer, A. Harutyunyan, M. H. Anderson, J. Liu, M. Geiselmann, B. Chazelas, S. Kundermann, S. Lecomte, M. Cecconi, A. Ghedina, E. Molinari, F. Pepe, F. Wildi, F. Bouchy, T. J. Kippenberg, and T. Herr, "A microphotonic astrocomb," Nat. Photonics **13**, 31 (2019).
17. M.-G. Suh, X. Yi, Y.-H. Lai, S. Leifer, I. S. Grudinin, G. Vasisht, E. C. Martin, M. P. Fitzgerald, G. Doppmann, J. Wang, D. Mawet, S. B. Papp, S. A. Diddams, C. Beichman, and K. Vahala, "Searching for exoplanets using a microresonator astrocomb," Nat. Photonics **13**, 25 (2019).
18. T. Herr, V. Brasch, J. D. Jost, I. Mirgorodskiy, G. Lihachev, M. L. Gorodetsky, and T. J. Kippenberg, "Mode spectrum and temporal soliton formation in optical microresonators," Phys. Rev. Lett. **113**, 123901 (2014).
19. J. K. Jang, M. Erkintalo, S. G. Murdoch, and S. Coen, "Observation of dispersive wave emission by temporal cavity solitons," Opt. Lett. **39**, 5503–5506 (2014).
20. C. Bao and C. Yang, "Stretched cavity soliton in dispersion-managed Kerr resonators," Phys. Rev. A **92**, 023802 (2015).
21. X. Dong, Q. Yang, C. Spiess, V. G. Bucklew, and W. H. Renninger, "Stretched-pulse soliton Kerr resonators," Phys. Rev. Lett. **125**, 033902 (2020).
22. S. K. Turitsyn, S. Bogdanov, and A. Redyuk, "Soliton-sinc optical pulses," Opt. Lett. **45**, 5352 (2020).
23. X. Xue, P. Grelu, B. Yang, M. Wang, S. Li, X. Zheng, and B. Zhou, *Dispersion-Less Kerr Solitons in Spectrally Confined Optical Cavities* (2021).
24. S. Zhang, T. Bi, and P. Del'Haye, *Microresonator Soliton Frequency Combs in the Zero-Dispersion Regime* (2022).
25. S. Ramelow, A. Farsi, S. Clemmen, J. S. Levy, A. R. Johnson, Y. Okawachi, M. R. E. Lamont, M. Lipson, and A. L. Gaeta, "Strong polarization mode coupling in microresonators," Opt. Lett. **39**, 5134 (2014).
26. Y. Li, J. Li, Y. Huo, M. Chen, S. Yang, and H. Chen, "Spatial-mode-coupling-based dispersion engineering for integrated optical waveguide," Opt. Express **26**, 2807–2816 (2018).
27. S.-P. Yu, D. C. Cole, H. Jung, G. T. Moille, K. Srinivasan, and S. B. Papp, "Spontaneous pulse formation in edgeless photonic crystal resonators," Nat. Photonics **15**, 461–467 (2021).
28. S. Kim, K. Han, C. Wang, J. A. Jaramillo-Villegas, X. Xue, C. Bao, Y. Xuan, D. E. Leaird, A. M. Weiner, and M. Qi, "Dispersion engineering and frequency comb generation in thin silicon nitride concentric microresonators," Nat. Commun. **8**, 372 (2017).
29. Ó. B. Helgason, F. R. Arteaga-Sierra, Z. Ye, K. Twayana, P. A. Andrekson, M. Karlsson, and J. Schröder, and Victor Torres-Company, "Dissipative solitons in photonic molecules," Nat. Photonics **15**, 305–310 (2021).
30. A. Tikan, J. Riemensberger, K. Komagata, S. Hönl, M. Churaev, C. Skehan, H. Guo, R. N. Wang, J. Liu, P. Seidler, and T. J. Kippenberg, "Emergent nonlinear phenomena in a driven dissipative photonic dimer," Nat. Phys. **17**, 604–610 (2021).
31. E. Lucas, S.-P. Yu, T. C. Briles, D. R. Carlson, and S. B. Papp, *Tailoring Microcombs with Inverse-Designed, Meta-Dispersion Microresonators* (2022).
32. G. Moille, X. Lu, J. Stone, D. Westly, and K. Srinivasan, *Arbitrary Microring Dispersion Engineering for Ultrabroad Frequency Combs: Photonic Crystal Microring Design based on Fourier Synthesis* (2022).
33. R. Szipöcs, K. Ferencz, C. Spielmann, and F. Krausz, "Chirped multilayer coatings for broadband dispersion control in femtosecond lasers," Opt. Lett. **19**, 201–203 (1994).
34. F. X. Kärtner, N. Matuschek, T. Schibli, U. Keller, H. A. Haus, C. Heine, R. Morf, V. Scheuer, M. Tilsch, and T. Tschudi, "Design and fabrication of double-chirped mirrors," Opt. Lett. **22**, 831–833 (1997).
35. D. Braje, L. Hollberg, and S. Diddams, "Brillouin-enhanced hyperparametric generation of an optical frequency comb in a monolithic highly nonlinear fiber cavity pumped by a CW laser," Phys. Rev. Lett. **102**, 193902 (2009).
36. E. Obrzud, S. Lecomte, and T. Herr, "Temporal solitons in microresonators driven by optical pulses," Nat. Photonics **11**, 600–607 (2017).
37. S.-P. Yu, H. Jung, T. C. Briles, K. Srinivasan, and S. B. Papp, "Photonic-crystal-reflector nanoresonators for Kerr-frequency combs," ACS Photon. **6**, 2083–2089 (2019).
38. G. H. Ahn, K. Y. Yang, R. Trivedi, A. D. White, L. Su, J. Skarda, and J. Vučković, "Photonic inverse design of on-chip microresonators," ACS Photon. **9**, 1875–1881 (2022).
39. J. Liu, G. Huang, R. N. Wang, J. He, A. S. Raja, T. Liu, N. J. Engelsen, and T. J. Kippenberg, "High-yield, wafer-scale fabrication of ultralow-loss, dispersion-engineered silicon nitride photonic circuits," Nat. Commun. **12**, 2236 (2021).
40. X. Ji, S. Roberts, M. Corato-Zanarella, and M. Lipson, "Methods to achieve ultra-high quality factor silicon nitride resonators," APL Photon. **6**, 071101 (2021).
41. M. Palamaru and P. Lalanne, "Photonic crystal waveguides: out-of-plane losses and adiabatic modal conversion," Appl. Phys. Lett. **78**, 1466–1468 (2001).
42. P. Lalanne and J. P. Hugonin, "Bloch-wave engineering for high-Q, small-V microcavities," IEEE J. Quantum Electron. **39**, 1430–1438 (2003).
43. C. Sauvan, G. Lecamp, P. Lalanne, and J. P. Hugonin, "Modal-reflectivity enhancement by geometry tuning in photonic crystal microcavities," Opt. Express **13**, 245–255 (2005).
44. V. Brasch, M. Geiselmann, T. Herr, G. Lihachev, M. H. P. Pfeiffer, M. L. Gorodetsky, and T. J. Kippenberg, "Photonic chip-based optical frequency comb using soliton Cherenkov radiation," Science **351**, 357–360 (2016).
45. D. C. Cole, A. Gatti, S. B. Papp, F. Prati, and L. Lugiato, "Theory of Kerr frequency combs in Fabry–Perot resonators," Phys. Rev. A **98**, 013831 (2018).
46. Y. K. Chembo and N. Yu, "Modal expansion approach to optical-frequency-comb generation with monolithic whispering-gallery-mode resonators," Phys. Rev. A **82**, 033801 (2010).
47. T. Hansson, D. Modotto, and S. Wabnitz, "On the numerical simulation of Kerr frequency combs using coupled mode equations," Opt. Commun. **312**, 134–136 (2014).
48. P. Del'Haye, A. Schliesser, O. Arcizet, T. Wilken, R. Holzwarth, and T. J. Kippenberg, "Optical frequency comb generation from a monolithic microresonator," Nature **450**, 1214–1217 (2007).

49. V. E. Lobanov, G. Lihachev, T. J. Kippenberg, and M. L. Gorodetsky, "Frequency combs and platicons in optical microresonators with normal GVD," Opt. Express **23**, 7713–7721 (2015).
50. X. Xue, Y. Xuan, Y. Liu, P.-H. Wang, S. Chen, J. Wang, D. E. Leaird, M. Qi, and A. M. Weiner, "Mode-locked dark pulse Kerr combs in normal-dispersion microresonators," Nat. Photonics **9**, 594–600 (2015).
51. P. Parra-Rivas, D. Gomila, E. Knobloch, S. Coen, and L. Gelens, "Origin and stability of dark pulse Kerr combs in normal dispersion resonators," Opt. Lett. **41**, 2402–2405 (2016).
52. A. W. Bruch, X. Liu, J. B. Surya, C.-L. Zou, and H. X. Tang, "On-chip $\chi^{(2)}$ microring optical parametric oscillator," Optica **6**, 1361–1366 (2019).
53. R. Wolf, Y. Jia, S. Bonaus, C. S. Werner, S. J. Herr, I. Breunig, K. Buse, and H. Zappe, "Quasi-phase-matched nonlinear optical frequency conversion in on-chip whispering galleries," Optica **5**, 872–875 (2018).
54. A. M. Perego, S. K. Turitsyn, and K. Staliunas, "Gain through losses in nonlinear optics," Light Sci. Appl. **7**, 43 (2018).
55. X. Lu, A. McClung, and K. Srinivasan, "High-Q slow light and its localization in a photonic crystal microring," Nat. Photonics **16**, 66–71 (2022).
56. B. G. Bale, J. N. Kutz, A. Chong, W. H. Renninger, and F. W. Wise, "Spectral filtering for mode locking in the normal dispersive regime," Opt. Lett. **33**, 941 (2008).
57. X. Dong, C. Spiess, V. G. Bucklew, and W. H. Renninger, "Chirped-pulsed Kerr solitons in the Lugiato-Lefever equation with spectral filtering," Phys. Rev. Res. **3**, 033252 (2021).